ASME Journal of Tribology
Online journal at:
https://asmedigitalcollection.asme.org/tribology

Rahul Gupta
Metallurgical Engineering and Materials Science,
Indian Institute of Technology, Powai,
Bombay 400076, India
e-mails: rahul.sliet2008@gmail.com;
rgupta20_phd17@thapar.edu

Tarun Nanda
Mechanical Engineering Department,
Thapar Institute of Engineering & Technology,
Patiala, Punjab 147001, India
e-mail: tarunnanda@thapar.edu

O. P. Pandey[1]
School of Physics and Materials Science,
Thapar Institute of Engineering & Technology,
Patiala, Punjab 147004, India
e-mail: oppandeytu@gmail.com

Varun Singhal
Department of Mechanical Engineering,
GLA University,
Mathura, Uttar Pradesh 281406, India
e-mail: v.singhal20@gmail.com

Sandeep Bansal
Department of Mechanical Engineering,
SGT University,
Gurugram, Haryana 147004, India
e-mail: sbansal440@gmail.com

Ravi Shankar Raman
Department of Mechanical Engineering,
ABES Engineering College,
Ghaziabad, Uttar Pradesh 201009, India
e-mail: ravi.raman21@gmail.com

Comparison of Tribological Characteristics of LM13/B_4C and LM13/Ilmenite Composites at High-Temperature Conditions

In this work, high-temperature tribological characteristics of ilmenite-reinforced LM13 aluminum alloy–based matrix composites (AMCs) and boron carbide–reinforced AMCs are compared. Stir-cast composites were processed using boron carbide (covalently bonded discontinuous particles (CDP)) and ilmenite (natural discontinuous particles (NDP)) particles separately as reinforcements. The particle size range was 106–125 μm, and reinforcement levels were 5, 10, and 15 wt% for both types of composites. Both composites exhibited a uniform distribution of reinforced particles and grain refinement. Compared to the LM13 base alloy, NDP composite containing 15 wt% reinforcement showed significant improvement in hardness (57%), coefficient of friction (57%), mild-to-severe wear transition temperature, average steady-state wear-rate (49%), and coefficient of thermal expansion (55%). CDP-15 composite showed slightly better properties than NDP-15 composite. Microstructure refinement, increased dimensional stability, formation of the oxide layer, and formation of tribolayer due to reinforcement of the ceramic fillers were the main reasons for the improvement in properties of processed AMCs. Scanning electron microscope (SEM)-energy dispersive spectroscopy (EDS) of wear tracks-debris showed abrasive/delamination wear as the main mechanism for materials loss. The research showed that the low-cost ilmenite particles can substitute for the very costly boron carbide particles as reinforcements in AMCs used for dry sliding wear applications under high operating temperatures–applied load conditions of the order of 300 °C–49 N.
[DOI: 10.1115/1.4063811]

Keywords: aluminum matrix composites, ilmenite, high-temperature wear, coefficient of thermal expansion, boron carbide, SEM-EDS, abrasion, dry friction, hardness, surface properties and characterization, wear mechanisms

1 Introduction

A lot of work has been reported in the last few years to improve the properties (mechanical/electrical/thermal) and tribological characteristics of metal matrix composites (MMCs) [1–4]. Lightweight alloys (viz. Al, Mg, and Ti based) are generally used as matrix material in MMCs [5,6]. These alloys have high specific stiffness, low corrosion rate, low weight-to-strength ratio, and low thermal coefficient expansion [7–9] but exhibit poor tribological characteristics [10–12]. Thus, to improve the wear behavior of lightweight alloys, MMCs are made, which are reinforced with discontinuous particles, viz. TiB_2, TiC, Al_2O_3, SiC, and WC [13–16]. Studies available on tribological characteristics of MMCs report their use as materials for connecting rods, cylinder liners, brake rotors, pistons, driving shafts, etc. [17,18]. Due to covalent bonding, discontinuous particles possess high hardness, temperature stability, and corrosion resistance [19]. Interestingly, there are some naturally occurring minerals, such as rutile (TiO_2), sillimanite (Al_2SiO_5), zircon ($ZrSiO_4$), and corundum (Al_2O_3), which exhibit similar properties [17,18,20]. These particles get formed under extreme conditions of pressure and temperature and display almost similar characteristics as are possessed by the covalently bonded particles [21,22]. It is reported that both these categories of particles when reinforced to metal-based matrices bring changes at a microstructural level and influence the wear characteristics of MMCs [13,20,23]. Under high-temperature conditions, these particles help in increasing the wear transition temperature of alloy–based matrix composites (AMCs) by providing thermal stability to the base alloy. In this regard, several studies are available that report the use of covalently bonded ceramic particle reinforcements such as B_4C, TiC, TiB_2, and ZrB_2 [24–27]. However, there are only limited studies available on the use of naturally occurring discontinuous particles as reinforcement in AMCs to improve the high-

[1]Corresponding author.

Contributed by the Tribology Division of ASME for publication in the Journal of Tribology. Manuscript received June 13, 2023; final manuscript received October 9, 2023; published online January 22, 2024. Assoc. Editor: Xiaolei Wang.

temperature wear behavior. Panwar and Pandey developed zircon-reinforced AMCs and reported superior high-temperature wear characteristics. An increase in transition temperature (from 150 °C to 250 °C) was noted at higher loadings (from 0 to 15 wt%) [28]. Sharma et al. studied the high-temperature wear characteristics of sillimanite-reinforced LM30 alloy and reported an increase in transition temperature from 150 °C to 200 °C [17]. Kumar et al. (2010) investigated an Al–Cu alloy–based MMC reinforced with TiB_2 particles (10 wt%) and reported an increase in working range from 0–100 °C to 0–300 °C [24]. Kumar et al. reported on the elevated temperature tribological behavior of the "AA5052 alloy + 9 vol% ZrB_2" composite and reported an increase in critical temperature from 100 °C to 150 °C [25]. To the best of our knowledge, the use of low-cost and naturally occurring ilmenite ($FeTiO_3$) particles for improving the high-temperature wear characteristics of MMCs is not available in the literature. Ilmenite is an ore of titanium, which is vastly present in coastal areas of Kerala, Odisha, Andhra Pradesh, and Tamil Naidu in the Indian subcontinent [29]. The properties possessed by ilmenite particles include high hardness (5–6 Mohs), high thermal stability, high chemical stability, and low thermal conductivity (1.49 W/mK). Several earlier studies reported in the literature show that the addition of ceramic-based oxides (TiO_2, ZrO_2, $ZrSiO_4$, Al_2SiO_5, etc.) enhances the mechanical properties and tribological characteristics of metal matrix composites [17,18,20,30]. Oxide-based particle reinforcement results in the establishment of a protective film over the sliding surface of MMCs [31–34]. Jafrey Daniel et al. investigated the mechanical/tribological characteristics of ZrO_2-reinforced Al2014 AMCs and reported improvements to a 6 wt% reinforcement level [35]. Patel et al. investigated the tribological/mechanical behavior of $ZrSiO_4$ particle (15 vol%) reinforced A4047 alloy–based AMCs and reported a significant increase in tensile strength/wear characteristics [36]. Alagarsamy and Ravichandran reported improvements in mechanical/tribological properties of TiO_2-reinforced AA7075 alloy–based AMCs till 10 wt% reinforcement level. Beyond 10 wt% reinforcement, properties deteriorated because of the agglomeration of particles [37].

The main objective of the present research was to improve the high-temperature wear characteristics of an Al–Si alloy by reinforcing naturally occurring discontinuous particles of ilmenite. The results obtained have been compared against the high-temperature wear behavior of B_4C-reinforced AMCs. The properties possessed by boron carbide particles are high hardness, low density, good chemical stability, and good strength, which make it a considerable candidate for enhancing the wear characteristic of AMCs in the case of covalently bonded discontinuous particles. This research also focuses on the investigation of the influence of different discontinuous particles (i.e., covalently bonded; B_4C and naturally occurring; ilmenite) on wear characteristics, friction behavior, and thermal properties of developed AMCs under elevated temperature conditions. The analysis of thermal properties was done to study the dimensional stability of fabricated AMCs at high-temperature conditions. Dimensional stability plays a crucial role in various industrial applications, such as cylindrical liners, brake rotors, pistons, and connecting rods. Thus, besides the study of high-temperature wear, there is a need to study the dimensional stability of AMCs by doing the analysis of the coefficient of thermal expansion (CTE).

2 Experimental Procedure

2.1 Materials. LM13 alloy is a matrix material and is available in the form of ingots. It is a near-eutectic Al–Si alloy used commercially for fabricating pistons. LM13 alloy was reinforced separately with (i) B_4C particles (representing covalently bonded ceramic reinforcement) and (ii) ilmenite particles ($FeTiO_3$ particles, representing naturally occurring ceramic reinforcement) to process the MMCs. Figures 1(*a*) and 1(*b*) present the scanning electron microscopy (SEM) images of ilmenite and boron carbide particles used in the present study. Both ilmenite and boron carbide particles appear to have an irregular morphology. The particle size range of reinforced particles was 106−125 μm, both for B_4C particles and $FeTiO_3$ particles. Table 1 presents the elemental composition of materials used for fabrication of the two different AMCs.

2.2 Processing of Aluminum Alloy-Based Matrix Composites. The preformed ingot of LM13 alloy was placed in a crucible, which was kept in a furnace (700 °C) to melt the ingot. Particles to be reinforced (B_4C or $FeTiO_3$) were kept for 30 min in a muffle furnace upheld at 450 °C to remove any volatile substance and to reduce the temperature gradient between molten alloy and reinforced particles. When LM13 alloy reached a complete molten state, a three-blade stirrer was used to blend the molten mass in a three-step process. In the first step, the molten LM13 alloy was stirred (650 rpm; 10 min). In the second step, the rotational speed was decreased to 250 rpm, and preheated reinforcement particles (B_4C or $FeTiO_3$) were injected into the molten mass. These AMCs were further made by varying the amount of reinforcement in three different weight percentages, viz. 5 wt%, 10 wt%, and 15 wt%. In the final step, stirring was continued (650 rpm; 10 min). The prepared molten slurry was poured into a mold made up of cast iron of dimensions $120 \times 120 \times 40$ mm^3 and allowed to cool in air. AMCs reinforced with naturally occurring discontinuous particles of ilmenite were designated as NDP, and the covalently bonded discontinuous particles of B_4C were designated as CDP. Table 2 presents the various formulations processed.

2.3 Characterization and Testing of Aluminum Alloy-Based Matrix Composites

2.3.1 Testing. Wear-rate, coefficient of thermal expansion, and hardness values were evaluated for the developed AMCs. From the casted billets, wear test samples were machined according to ASTM G99 standard [38]. In ASTM G99 standard, a test specimen of a given composition is fabricated as a cylindrical pin of 8 mm diameter (d) and 90 mm height (h). Wear testing was conducted

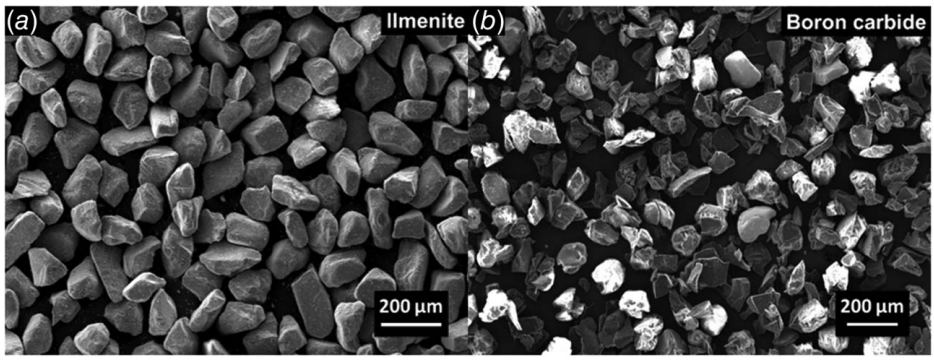

Fig. 1 SEM images of (*a*) ilmenite and (*b*) boron carbide particles

Table 1 Chemical constitution of matrix material and reinforced particles

Materials	Chemical composition (wt%)										
	Si	Ni	Cu	Fe	Mn	Ti	Mg	Al	O	B	C
LM13 alloy	12.0	1.20	1.10	0.80	0.40	0.18	0.11	84.21	–	–	–
Ilmenite ($FeTiO_3$)	–	–	–	15.37	–	36.93	–	–	47.70	–	–
Boron carbide (B_4C)	–	–	–	–	–	–	–	–	–	67.96	32.04

Table 2 Composition of different AMCs made by using B_4C and ilmenite

Fabricated composites	Sample code and reinforcement level (wt%)		
	5	10	15
LM13 alloy reinforced with natural discontinuous particles i.e., ilmenite particles	NDP-5	NDP-10	NDP-15
LM13 alloy reinforced with covalently bonded discontinuous particles i.e., boron carbide particles	CDP-5	CDP-10	CDP-15

Note: NDP: natural discontinuous particles and CDP: covalently bonded discontinuous particles.

under dry sliding conditions (against hardened EN31 steel disc), both for ambient temperature and elevated temperature conditions (100 °C, 200 °C, and 300 °C). High-temperature wear test was done in a closed container attached to three electric heaters (to reach operating temperatures till 400 °C). Container temperature was monitored using thermocouples. The applied load was varied as 9.8 N, 29.4 N, and 49.0 N. For each wear test, the sliding distance was varied from 0 to 3000 m, and the sliding speed was selected as 1.6 m/s. These test conditions were selected from earlier reported work of our research group [18,20]. Loss in height (h_l) of cylindrical pin due to relative sliding between counter-surfaces was measured using linear variable differential transformer (LVDT) sensors attached to the pin-on-disc setup. Using this height loss (h_l), the total volume loss (V_l) was calculated. Finally, wear-rate was calculated as per Eq. (1) by determining volume loss (V_l) and sliding distance (d_s).

$$\mathrm{WR} = \frac{\pi \times d^2 \times h_l}{4 \times d_s} \tag{1}$$

The tangential force acting on the sliding surface was determined using a stress sensor. By dividing this tangential force value with a particular applied load condition, the coefficient of friction (COF) value was obtained. With this method, COF values were obtained over the entire sliding distance. The average of all such values represented the COF of particular AMCs under a specific testing condition.

A surface roughness tester was used to determine the surface roughness (R_a) value of samples before as well as after the wear tests/friction tests. For roughness measurements, trace length and cutoff length were 1.25 mm and 0.25 mm, respectively.

Thermal analysis of AMCs was done by obtaining thermal strain values and CTE values using a dilatometer. Cylindrical samples of dimensions $6 \times 6 \times 4$ mm^3 were used for the purpose. For thermal analysis, the temperature of the chamber was increased from 50–300 °C at a heating rate of 5 °C/min, and a change in the length of the sample (ΔL) was recorded with respect to the rise in temperature. Change in length (ΔL) divided by the original length (L) of the sample provided the thermal strain of AMCs. Further, considering "ΔT" as a change in operating temperature, the CTE value was obtained as given in Eq. (2):

$$\mathrm{CTE} = \frac{\Delta L}{L \times \Delta T} \tag{2}$$

The hardness of AMCs was measured using a Rockwell hardness tester (on a B scale). The load applied for hardness testing and dwell time were 100 kgf and 10 s, respectively. A tempered steel ball indenter of 1.58 mm diameter was used.

2.3.2 Characterization. Wear test samples were used for optical microscopy also. The surface of samples was flattened and mirror-polished according to the standard metallurgical procedure. Phase changes were determined using X-ray diffraction (XRD). In XRD, Cu K_α radiation was used, and the scanning range for the sample was kept in the range of 20–90 deg. SEM with an attachment for electron dispersive spectroscopy (EDS) was used on wear tracks-debris to predict the wear mechanism.

3 Results and Discussion

3.1 X-Ray Diffraction Analysis. Figure 2 presents the XRD graph of AMCs containing 15 wt% of boron carbide (i.e., CDP-15) and 15 wt% of ilmenite (i.e., NDP-15).

X-ray diffraction analysis of CDP-15 and NDP-15 revealed the presence of aluminum and silicon, which are consistent with the base alloy. Additionally, various other elements and compounds were detected, indicating the formation of intermetallic compounds, the occurrence of interfacial reaction products, and/or the existence of reinforced particles. CDP-15 composites exhibited extra peaks of phases of boron carbide, nickel, and intermetallic aluminum–nickel. On the other hand, NDP-15 composites revealed the occurrence of extra peaks corresponding to ilmenite, silicon oxide, iron

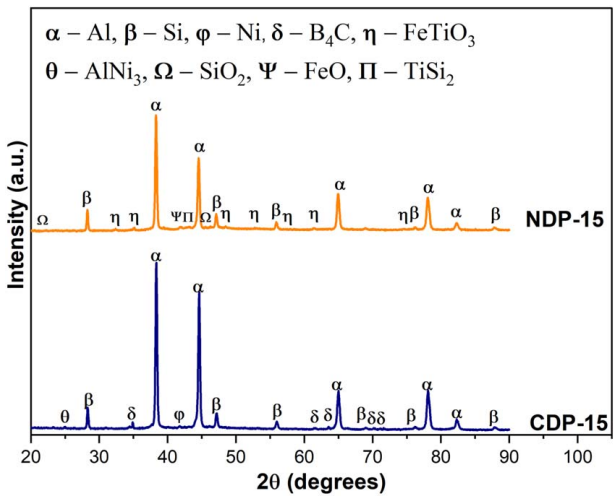

Fig. 2 XRD pattern of NDP-15 and CDP-15 composites

oxide, and intermetallic titanium–silicon. The production of an intermetallic compound of aluminum–nickel was only observed for CDP composites. Further, the presence of nickel phase in CDP composites is attributed to the alloying element present in the base alloy, as shown in Table 1. In NDP composite, iron oxide, silicon oxide, and intermetallic titanium–silicon correspond to the interfacial products. These products were formed due to the reaction between reinforced particles (ilmenite) and the matrix material (silicon of the base alloy). The interfacial reaction is described in Eq. (3).

$$3Si + FeTiO_3 \rightarrow FeO + SiO_2 + TiSi_2 \quad (3)$$

There was no evidence of any interfacial reaction in CDP composites. Various researchers have stated that better wetting characteristics are obtained when interfacial reaction products are formed on the reinforced particles [39–41]. Therefore, a strong interfacial bond is formed by the ilmenite particles, which could potentially be attributed to the presence of interfacial products in the case of NDP composites.

3.2 Microstructure Evolution. Microstructure obtained in MMCs depends on (i) the difference in thermal conductivities of reinforced particles and the base alloy and (ii) the distance between two adjacent reinforced particles in the metal matrix [18,42,43]. The microstructure of LM13 alloy consisted of primary aluminum and an eutectic mixture of aluminum and silicon (Fig. 3(*a*)).

Due to variations in the thermal conductivity of reinforced particles, there exists a thermal gradient near the reinforced particles. This nonuniform temperature distribution was attributed to the difference in thermal conductivity values of matrix and reinforced particles. Thermal conductivity values of boron carbide, ilmenite, and LM13 alloy are 30 W/mK, 1.49 W/mK, and 166 W/mK, respectively [33,44]. During the cooling of the composites, the reinforced particles created a temperature difference within the molten mass due to their lower thermal conductivity value and heat dissipation capability as compared to LM13 alloy. Molten mass around the reinforced particles remained at a higher temperature, which forces the nucleation of primary Al at a distance from the reinforced particles [18,43,45]. With the increase in reinforcement level, the distance between adjacent reinforced particles decreased. This decreased the growth of primary Al nuclei. On reaching the eutectic temperature, the hot molten matter around the particles started to solidify and resulted in the nucleation of the eutectic mixture. For this reason, reinforced particles were surrounded by eutectic mixture, as shown in Figs. 3(*f*) and 3(*g*). The reinforced particles also provided a hindrance to the growth of eutectic Si. This hindrance helped in refining the grain size of primary Al and also of eutectic silicon (Figs. 3(*f*) and 3(*g*)). By using IMAGEJ software, the size of primary Al and eutectic silicon was obtained for LM13 alloy ($140 \pm 21.01\ \mu$m, $39.96 \pm 10.77\ \mu$m), NDP-15 composite ($59.66 \pm 7.78\ \mu$m, $7.04 \pm 2.59\ \mu$m), and CDP-15 composite ($38.63 \pm 5.78\ \mu$m, $5.46 \pm 1.55\ \mu$m), respectively. The lower size of primary aluminum and silicon is observed for composites, which are reinforced with boron carbide particles. This behavior was attributed to the lower density of boron carbide particles (i.e., 2.52 g/cm^3) in comparison to ilmenite particles (i.e., 4.72 g/cm^3) [1,46]. For a particular region of AMCs, reinforcement having lower density will have a greater number of reinforced particles, which leads to decrement in the distance between the adjacent reinforced particles (Figs. 3(*c*) and 3(*e*)). Thus, the distance between adjacent reinforced particles is less in the case of the CDP-15 composite when compared to the NDP-15 composite. This decrease in distance results in a higher restriction to the growth of grains, which corresponds to finer grains for the CDP-15 composite.

3.3 Hardness Testing of Aluminum Alloy-Based Matrix Composites. Table 3 provides the hardness obtained for various composites.

The hardness of the base alloy was determined as 45.04 ± 3.18 HRB. AMCs showed higher hardness values than the base alloy. At a given reinforcement level, both types of AMCs showed comparable values of hardness. During hardness testing, the indentation obtained on the specimen's surface under the effect of load resulted in localized plastic deformation of the material. For the unreinforced base alloy, the indenter caused a high degree of localized plastic deformation in the absence of particle reinforcement. However, during hardness testing of AMCs, there was a decrease in localized plastic deformation due to the presence of hard B_4C or ilmenite particles. Further, for a given AMC, the increase in hardness values was observed with the rise in weight percentage of reinforced particles. This was a result of reduced inter-particle distance, causing resistance to plastic deformation [15].

During hardness testing, compressive force allows the material to flow in a vertical direction. This vertical flow of material causes the reinforced particles to concentrate beneath the indenter, as shown in Fig. 4. The increase in the concentration of particles below the indenter leads to the transfer of load from the matrix to the reinforced particles. Also, plastic deformation of matrix material decreases with a decrease in inter-particle distance [47]. The pattern of plastic deformation in the unreinforced base alloy is uniform, as there is no reinforcement. However, the presence of reinforced particles in composites fragments the field of plastic deformation. This fragmentation corresponds to the nondeformability of reinforced particles, causing an increase in resistance to plastic deformation of matrix material [47]. Due to these reasons, the hardness of AMCs shows a rising trend with an increase in the content of reinforced particles. Further, these factors also depend on the number of particles present in an AMC at a given reinforcement level. This aspect has a direct correlation with the density of particles at a given reinforcement level. Due to the high number of particles in CDP composites at particular reinforcement levels, the field of plastic deformation is highly fragmented, which causes higher restrictions on the plastic deformation of the matrix. For this reason, at a given reinforcement level, B_4C particle-based AMCs showed higher hardness than ilmenite-reinforced AMCs.

3.4 Coefficient of Thermal Expansion. Figures 5(*a*)–5(*f*) present the "thermal strain versus operating temperature" and "CTE versus operating temperature" graphs for base alloy and various AMCs. The operating temperature was varied in the range of 50–300 °C. Experimentally, CTE values were calculated as per Eq. (2).

For any AMC composition at any given operating temperature, thermal strain/CTE values were lower as compared to those of the base alloy. Also, CTE values of AMCs at a given operating temperature decreased with increased reinforcement levels (Figs. 5(*d*) and 5(*f*)). The results showed that the injection of reinforced particles to LM13 alloy decreased the CTE of resulting AMCs. Thus, particle addition is useful to tailor the CTE value of LM13 alloy. CDP-15 and NDP-15 showed the highest reduction in average CTE values (37.58% and 48.51%, respectively, over the base alloy). During the heating of AMCs, the presence of reinforcement restricts the expansion of matrix material due to different CTE of matrix and reinforced particles. This restriction to expansion causes a decrease in the CTE of AMCs [18]. It may be noted that the relatively lower average CTE value obtained for NDP composites indicated a high strength of interfacial bonding formed by the combination of matrix–reinforcement in comparison to CDP composites [17,48].

For an increase in temperature in the range of 50–100 °C, the CTE value of AMCs increased (for both types, viz., CDP as well as NDP composites). However, with a further rise in temperature (i.e., in the range of 100–300 °C), the trend observed in CTE

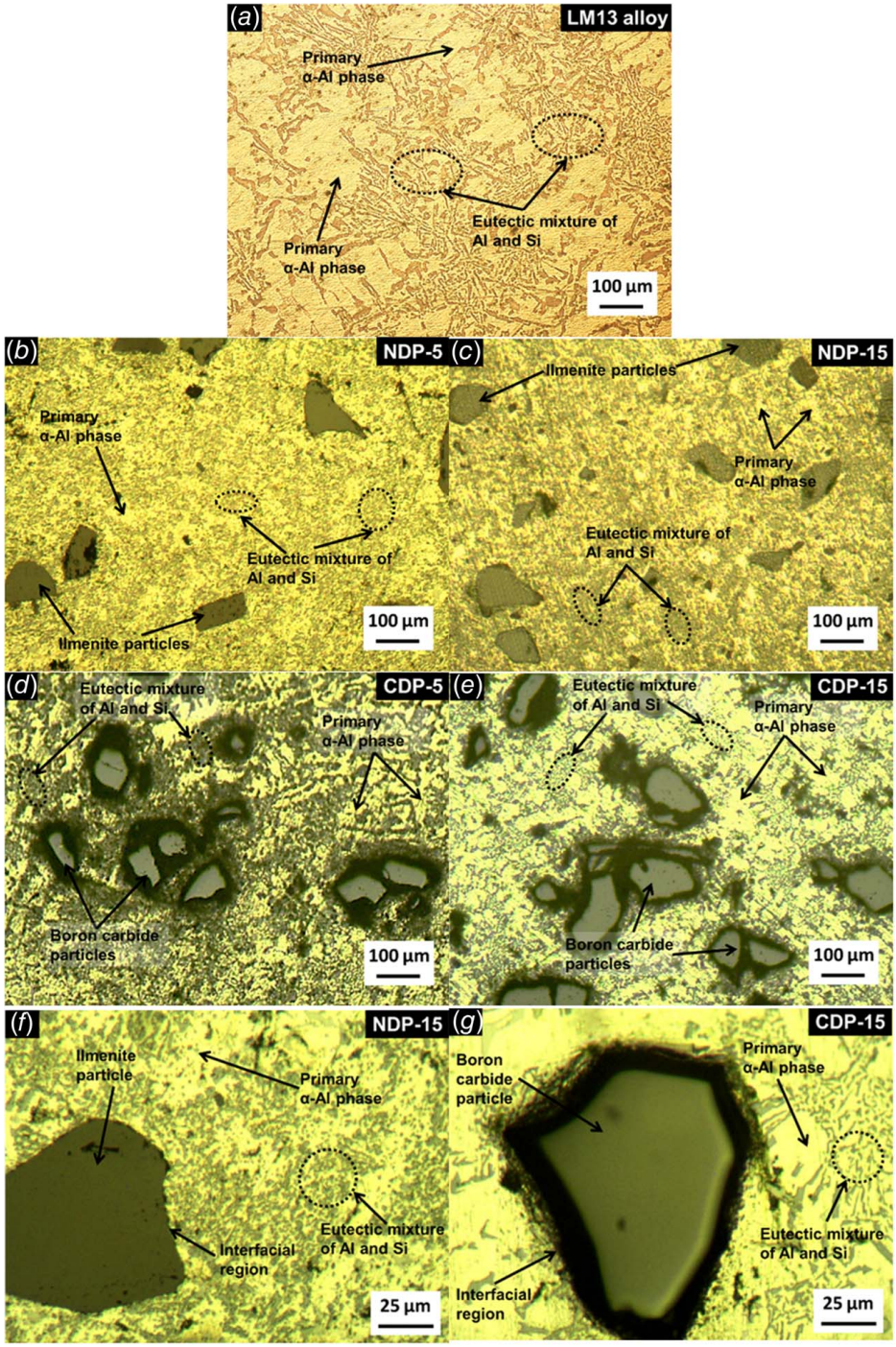

Fig. 3 Microstructures of (*a*) LM13 alloy and composites (*b*) NDP-5, (*c*) NDP-15, (*d*) CDP-5, and (*e*) CDP-15 at a magnification of 100X and optical micrographs of (*f*) NDP-15 and (*g*) CDP-15 composites at magnification of 500X showing interfacial region and grains of aluminum and silicon

values with temperature was different for the two types of AMCs. In this temperature range (100–300 °C), CDP composites showed a decreasing trend in CTE values, whereas NDP composites continued to show an increasing trend with an increase in temperature. Generally, with an increase in operating temperature, the thermal strain increases significantly and results in an increase in the CTE value of AMCs. This general behavior was displayed by the base alloy as well as NDP composites in the present research. However, for CDP composites, a decrease in CTE values with an increase in temperature in the range of 100−300 °C is a typical behavior reported earlier also in the literature [49,50]. For the CDP composites (i.e., AMCs containing covalently bonded ceramic particles like SiC and B_4C), in addition to the thermal strain factor, the stress level in AMCs also governs the change in CTE as a function of temperature [49]. From the results, it may be interpreted that for the initial increase in temperature (50 −100 °C), tensile stress acted on the matrix causing an increase in CTE. However, for the temperature change in the high-temperature regime (100−300 °C), the stress on the matrix changed to compressive, resulting in a decrease in CTE values. Further, it is well reported in the literature that the increase in solid solubility of silicon in aluminum shows a negative effect on the thermal

Table 3 Rockwell hardness values for AMCs

Reinforcement level in AMCs (wt%)	Rockwell hardness value (HRB) for AMCs reinforced with	
	Covalently bonded discontinuous particles (B_4C)	Natural discontinuous particles ($FeTiO_3$)
	CDP composites	NDP composites
5	60.57 ± 4.35	59.33 ± 3.01
10	67.57 ± 4.19	65.66 ± 4.79
15	70.42 ± 3.50	67.83 ± 3.50

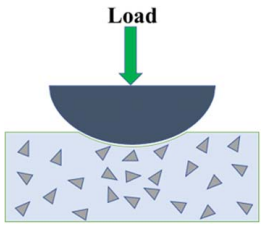

Fig. 4 Variation of particle concentration in AMCs during hardness testing

expansion of AMCs [49,50]. This factor also resulted in a decrease in CTE values of CDP composites with an increase in temperature in the high-temperature regime (100–300 °C). The results indicated that the presence of ilmenite in NDP composites, however, suppressed the Si solubility factor, and so, these AMCs continued to show an increase in CTE values with an increase in temperature (for the entire range, 50–300 °C). The XRD analysis of NDP-15 composites shows the occurrence of interfacial reaction between silicon and ilmenite particles. This signifies the greater affinity of ilmenite particles for silicon present in the LM13 base alloy, which is considered as a possible reason for the restriction to the solubility of silicon in aluminum. However, no such interfacial reaction is observed in the case of CDP-15 composites, which could be attributed to an increase in the solid solubility of silicon in aluminum. In the case of LM13 alloy, CTE value is mainly affected by the restriction caused by silicon grains to the expansion of aluminum. Further, this restriction to the expansion of aluminum depends upon the specific area of contact between aluminum and silicon [51]. From microstructural analysis, the higher grain size of silicon in LM13 alloy signifies the lower specific area of contact. The lower specific area of contact is attributed to the lower restriction to expansion caused by silicon, which results in a higher CTE value.

3.5 Coefficient of Friction and Wear Characteristics Under Elevated Temperature Conditions. COF values and wear-rate behavior of CDP and NDP composites for different reinforcement levels, applied loads, and operating temperatures are shown in Figs. 6 and 7, respectively. COF value and average steady-state wear-rate of the pin surface of base alloy/AMCs were obtained for each operating temperature. For obtaining the average steady-state wear-rate at a given temperature, the wear-rates obtained in the sliding distance range of 1500–3000 m were considered. Several earlier studies have also reported the attainment of steady-state wear in the sliding distance range of 1500–3000 m for ceramic particle–reinforced AMCs [17,20].

Figures 6(*a*) and 7(*a*) present the COF values and the average wear-rate values of LM13 alloy at various operating temperature–applied load conditions. For all applied load conditions, an increasing trend in COF and wear-rate was observed with an increase in AT (for the entire range). High applied load–operating temperature resulted in the rupturing of the oxide layer and thermal softening of the composite pin, causing a gradual increase in wear-rate till 100 °C. For higher temperatures (>100 °C), the increase in wear-rate was sharper. Thus, for all applied load conditions, the transition from mild to severe wear for base alloy was seen at an operating temperature of 100 °C. At high operating temperature–applied load condition of 300 °C–49.0 N, the LM13 alloy test sample got excessively worn out at a sliding distance of 1850 m (test could not be run beyond this sliding distance i.e., from 1850 m to 3000 m as the stylus of LVDT sensor reached its maximum limit because of excessive wear and thus stopped indicating further reading of height loss). Due to this, data required for calculations remained unavailable, and thus, data under 300 °C–49.0 N were not added to the wear graphs.

Figures 7(*b*) and 7(*g*) present the average wear-rates for various AMCs for different operating temperatures. Similar to the trend observed for LM13 alloy, a continuous rise in wear-rate was seen for AMCs with an increase in temperature (for the entire spectrum of 50–300 °C) under each applied load condition. However, the following differences were noted: (i) for any applied load–operating temperature condition, AMCs showed a lower average steady-state wear-rate in comparison to LM13 alloy, (ii) for any applied load–operating temperature condition, the average wear-rate of AMCs reduced with the rise in reinforcement level (higher reinforcement level reduced the CTE of AMCs causing improved thermal stability and hence lower wear-rates), (iii) mild-to-severe transition temperature for AMCs was higher (200 °C) than that for the base alloy (100 °C), and finally (iv) compared to the base alloy where at 300 °C–49 N condition, complete wear was observed at 1850 m, the AMCs were able to withstand this extreme condition.

Table 4 presents the percentage decrease in average wear-rate and COF values of AMCs compared to LM13 alloy at the mild-to-severe transition temperature of 200 °C.

Maximum reduction in wear-rate for AMCs was shown by CDP-15 composite (61% reduction over base alloy under 9.8 N load condition) and NDP-15 composite (52% reduction over base alloy). The addition of reinforced particles resulted in the refinement of grains of primary aluminum and eutectic silicon present in the matrix material. This provided increased grain boundary area in AMCs, resulting in more restriction to the movement of cracks generated during sliding wear [52]. The restriction to the propagation of cracks reduced the tendency for convergence of cracks, resulting in the removal of material at a slower rate. As discussed earlier, reinforced particles also reduced the CTE of resulting AMCs causing reduced wear-rates. Thus, the expansion of LM13 alloy is highly restricted by the boron carbides and ilmenite particles, which enhances the dimensional stability and slows down the softening of LM13 alloy at high-temperature conditions (Fig. 5). The increase in dimensional stability and lesser softening of LM13 alloy help in decreasing the transfer of matrix material from pin surface to steel counter surface [17]. Hence, the lower CTE of AMCs at high-temperature conditions results in high wear resistance when compared to LM13 alloy. During wear testing, sliding surfaces got heated up due to frictional force acting between both the counter-surfaces. Due to the lower thermal conductivity of reinforced particles (ilmenite particles: 1.49 W/mK; boron carbide particles: 30 W/mK), a high-temperature zone got created at the contact surfaces, which leads to the establishment of oxide layer on the sliding surface. This prevents direct metal-to-metal contact, which helps in reducing the wear-rates of AMCs [33,44,53]. For these reasons (grain

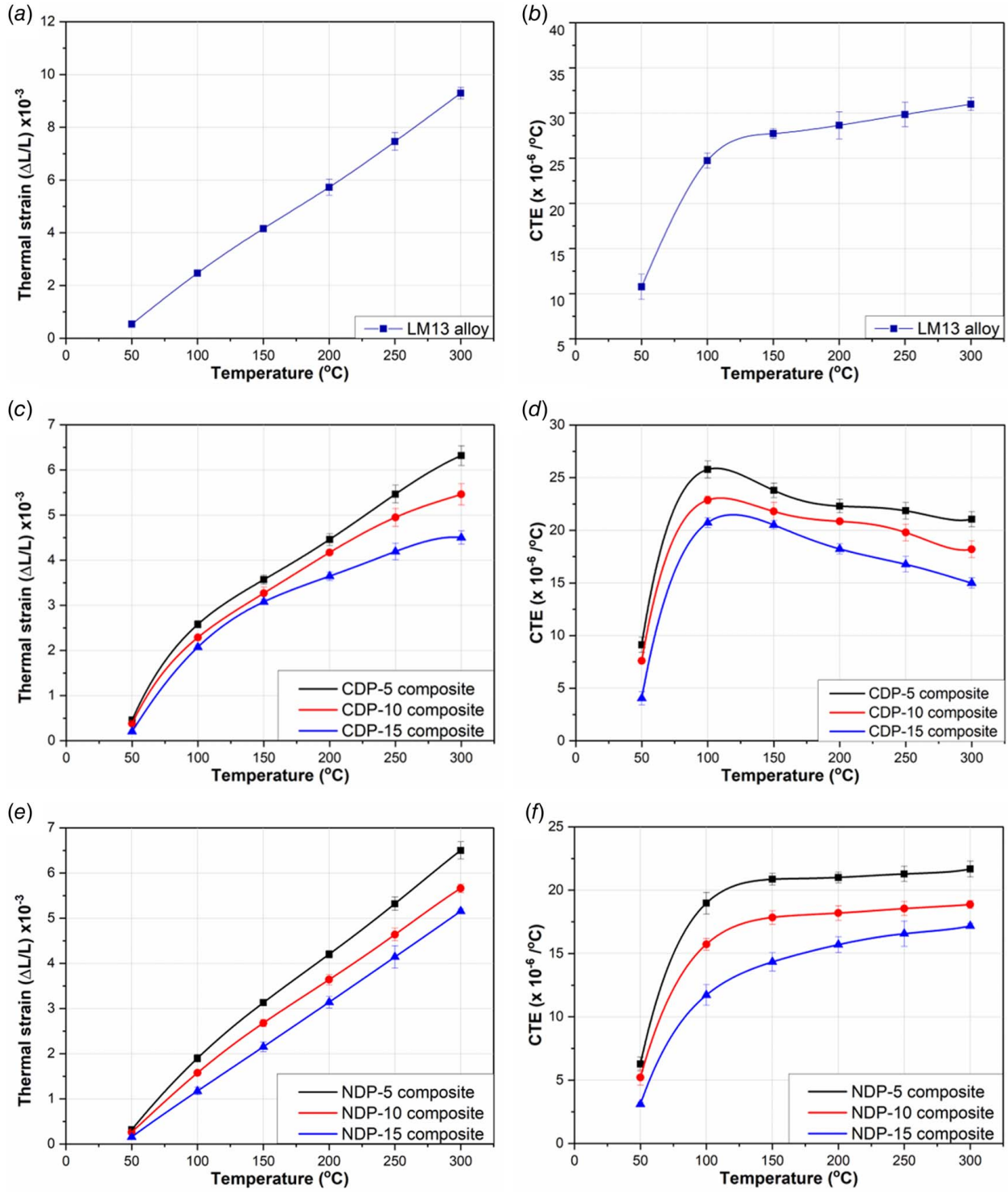

Fig. 5 Variation in thermal strain and CTE values as a function of operating temperature for (*a*) and (*b*) LM13 base alloy, (c) and (*d*) CDP composites, and (e) and (*f*) NDP composites

refinement, lower CTE value, and lower thermal conductivity due to addition of reinforced particles to AMCs), the COF values and average steady-state wear-rate continuously reduced with an increase in reinforcement level in AMCs for a given applied load–operating temperature condition.

Finally, the average steady-state wear-rate of CDP-15 and NDP-15 composites was compared for all operating temperature–applied load conditions using Fig. 7 and Table 4. Wear-rate behavior of both materials was comparable.

Figure 8 presents the rate of change of wear-rate with respect to change in operating temperature over the range of ambient temperature to 300 °C. Figures 8(*a*)–8(*c*) show that for any given value of derivative of wear-rate w.r.t. operating temperature, the wear performance of both the AMCs is comparable and far superior to the base alloy. For example, in Fig. 8(*a*) (for applied load condition of 9.8 N), at a derivative value of 0.025 mm^3m^{-1} $°C^{-1}$, NDP-15 and CDP-15 can operate till high temperatures of about 215 °C (corresponding to point "b") and 255 °C (corresponding

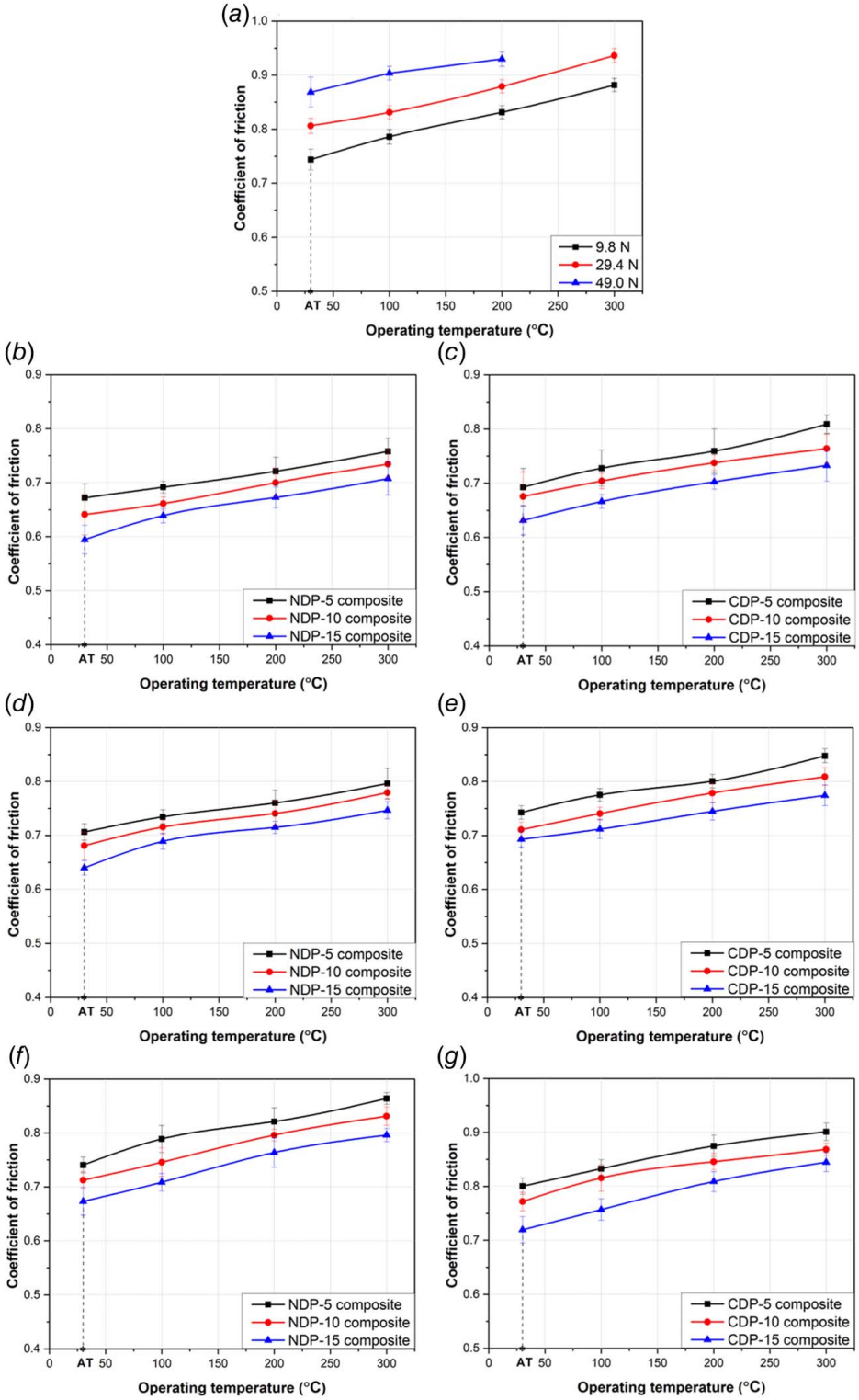

Fig. 6 Variation in COF values versus operating temperature for (*a*) LM13 alloy at different applied load conditions, (*b*) NDP composites at 9.8 N load, (*c*) CDP composites at 9.8 N load, (*d*) NDP composites at 29.4 N load, (*e*) CDP composites at 29.4 N load, (*f*) NDP composites at 49.0 N load, and (*g*) CDP composites at 49.0 N load; AT represents the ambient temperature conditions

to point "c"), whereas the base alloy specimen can operate till a relatively low temperature of about 105 °C only (corresponding to point "a"). Based on these data, it can be concluded that both types of AMCs can work nearly at the same operating temperature. Though CDPs are slightly superior to NDPs in the context of resistance shown to wear, however, the natural mineral ilmenite used in NDPs has very less cost (price of boron carbide particles used in CDPs is about 25 times more than price of ilmenite used in NDPs). Further, ilmenite and boron carbide have comparable densities (ilmenite: 4.72 g/cm^3; boron carbide: 2.52 g/cm^3). Considering these aspects (comparable wear-rate till elevated temperatures of 300 °C and significant price reduction), NDP composites appear

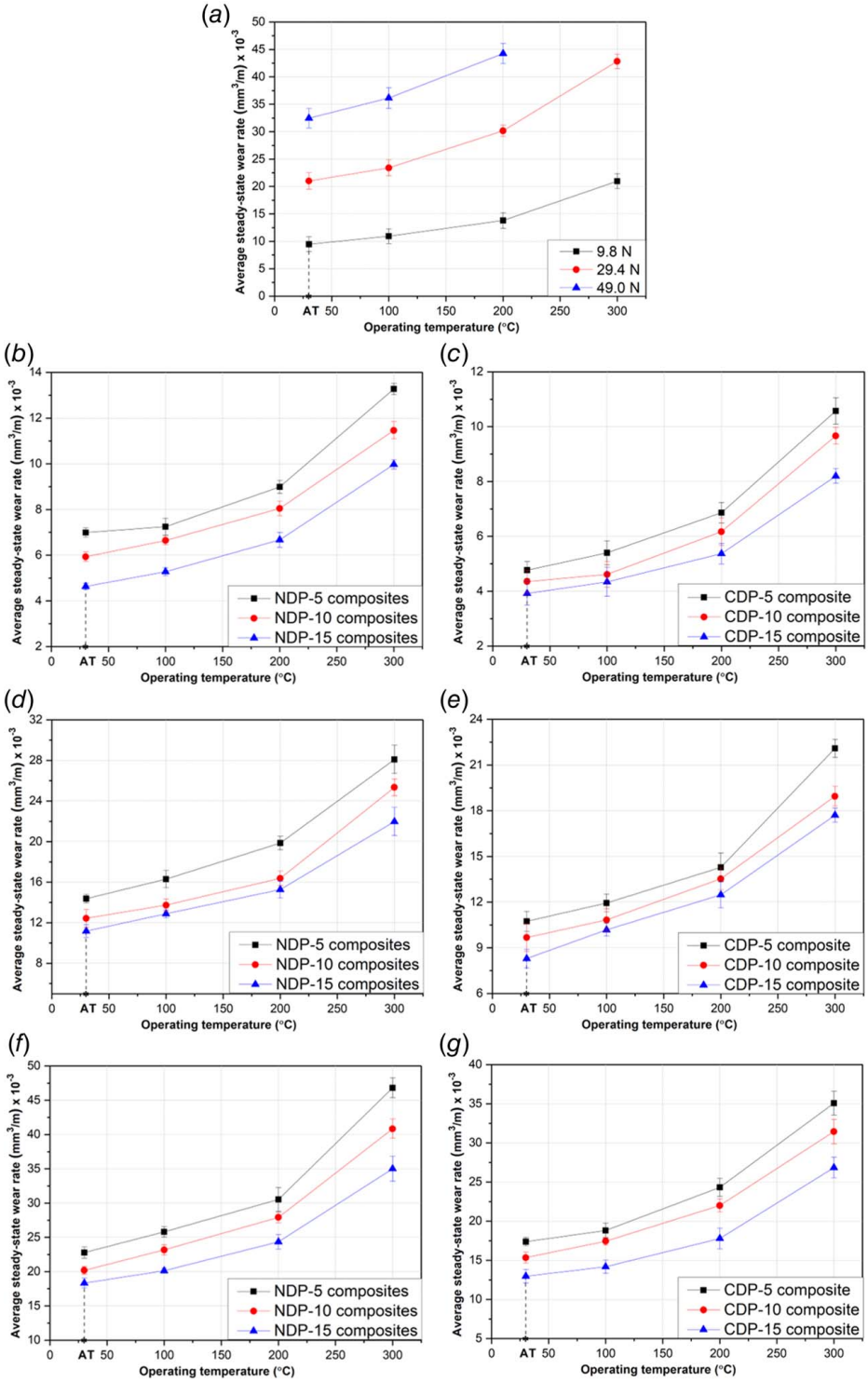

Fig. 7 Variation in average wear-rate versus operating temperature for (*a*) LM13 alloy at different applied loads, (*b*) NDP composites at 9.8 N load, (c) CDP composites at 9.8 N load, (*d*) NDP composites at 29.4 N load, (e) CDP composites at 29.4 N load, (*f*) NDP composites at 49.0 N load, and (*g*) CDP composites at 49.0 N load; AT represents the ambient temperature conditions

to be a better material for processing brake rotors, pistons, and cylinder liners for light vehicles.

3.6 Worn Surface and Debris Analysis. Worn surfaces obtained after the wear test for CDP and NDP composites comprised of three different constituent regions, viz. plowing region, delamination region, and mechanical mixed layer (MML). Worn surfaces of CDP-15 and NDP-15 are shown in Figs. 9(*a*) and 9(*c*), respectively, for the operating condition at 200 °C–9.8 N. Both types of AMCs showed the presence of abrasive grooves on the sliding surface (i.e., plowing region). This plowing region signified the entrapment of fractured asperities between the counter-surfaces.

Table 4 Percentage decrease in average wear-rate and COF values of AMCs with reference to LM13 alloy at mild-to-severe transition temperature

Applied load condition (N)	Percentage reduction					
	NDP composite at a given reinforcement level (wt%)			CDP composite at a given reinforcement level (wt%)		
	5	10	15	5	10	15
9.8	35 (13)	42 (16)	52 (19)	50 (9)	55 (11)	61 (15)
29.4	34 (14)	46 (16)	49 (19)	53 (9)	55 (11)	59 (15)
49.0	31 (12)	37 (14)	45 (18)	45 (6)	50 (9)	60 (13)

Note: Percentage reduction values are presented as X (Y), where X represents percentage reduction in average steady-state wear-rate, and Y represents percentage reduction in COF values.

Grooves observed were slightly shallower for CDP-15 when compared to NDP-15 composite. This was attributed to microstructure refinement in CDPs, which resulted in better fracture toughness/hardness. EDS analysis of worn surfaces of CDP-15 and NDP-15 is presented in Figs. 9(*b*) and 9(*d*), respectively. The existence of iron and carbon content on the sliding surface signifies the transfer of material (Fe and C) from the steel disc to the surface of the AMC pin. Further, aluminum, silicon, titanium, and oxygen were also observed on the sliding surfaces. The source of titanium observed on the worn surface of NDP-15 was the reinforced ilmenite particles ($FeTiO_3$). The nontraceability of boron on the worn surface of B_4C particle–reinforced CDP-15 was attributed to the low atomic number of boron. The presence of oxygen on the wear tracks of both the AMCs proved that the sliding surfaces oxidized as a result of applied load and temperature. However, the presence of higher oxygen (6% more) and iron contents (i.e., 93% more) in CDP-15 compared to NDP-15 signified the presence of a more stable MML on the surface of CDPs.

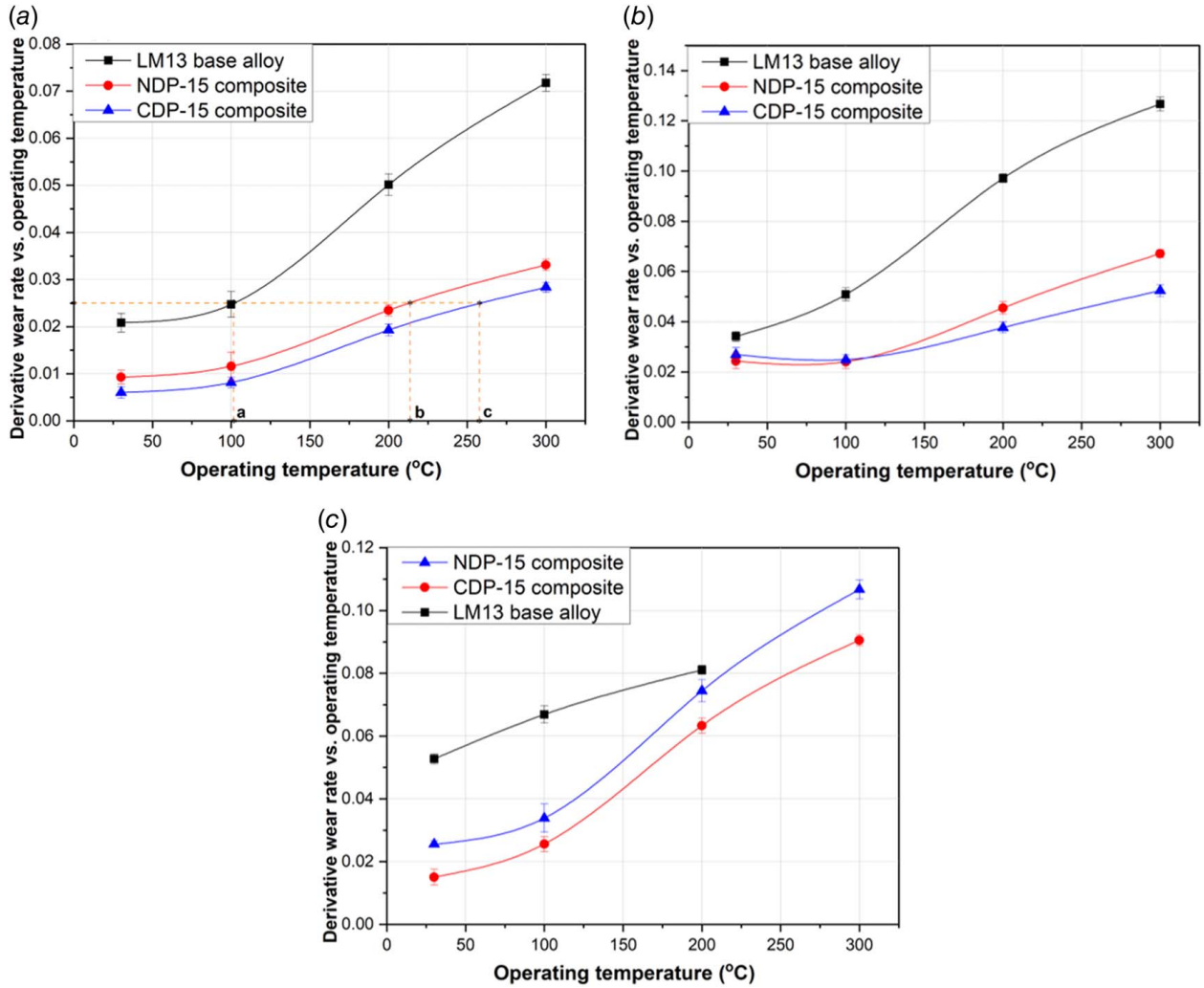

Fig. 8 Derivative of wear-rate versus operating temperature at an applied load of (*a*) 9.8 N, (*b*) 29.4 N, and (*c*) 49.0 N for LM13 base alloy, NDP-15 composite, and CDP-15 composite

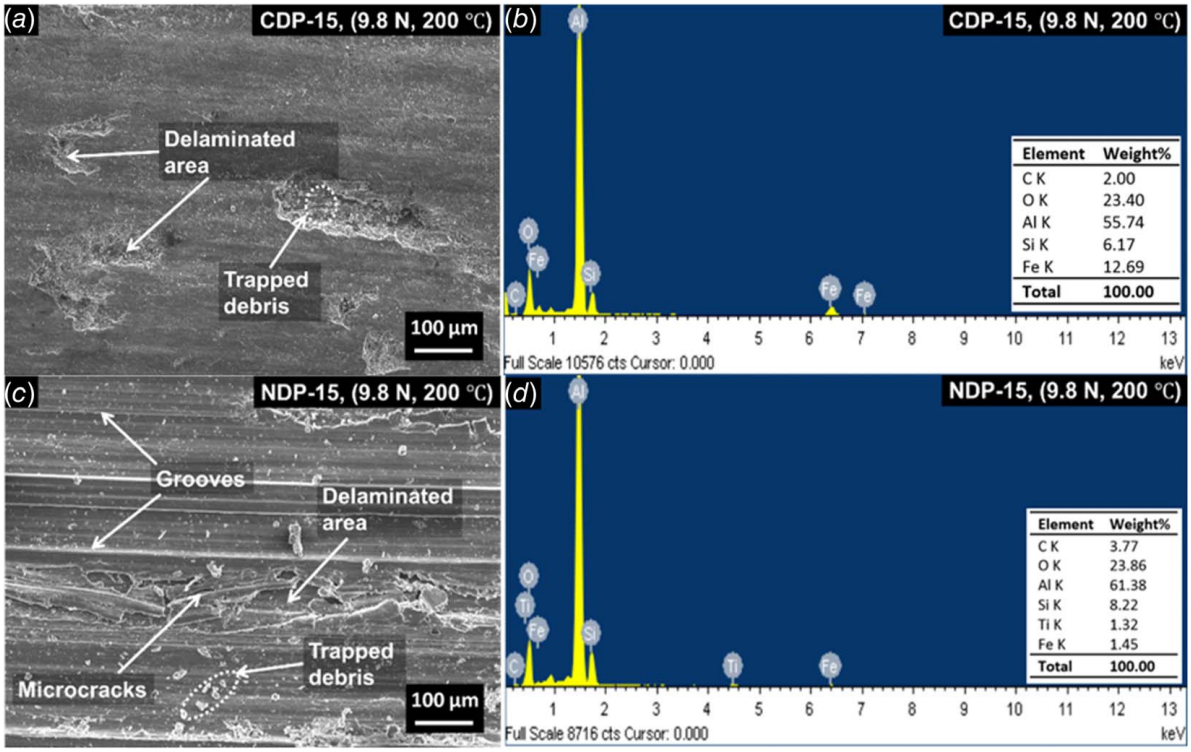

Fig. 9 SEM-EDS of wear track of (*a*) and (*b*) CDP-15 and (*c*) and (*d*) NDP-15 obtained at 9.8 N and 200 °C condition

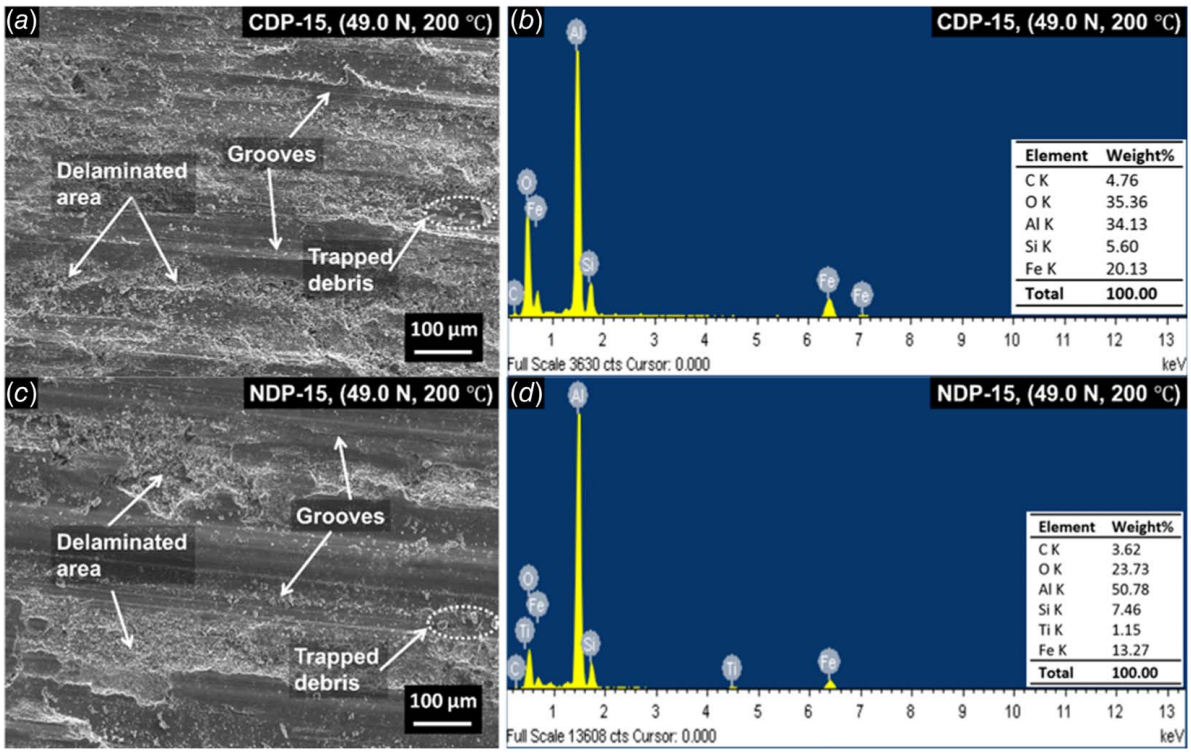

Fig. 10 SEM-EDS of wear track of (*a*) and (*b*) CDP-15 and (c) and (*d*) NDP-15 obtained at 49 N and 200 °C condition

Figure 10 presents the SEM-EDS images of the worn surface of CDP-15 and NDP-15 under the operating condition of 200 °C–49.0 N. Worn surfaces of both types of AMCs showed the presence of craters and abrasive grooves (Figs. 10(*a*) and 10(*c*)).

The presence of craters on the sliding surfaces was attributed to the generation and subsequent convergence of cracks under the high applied load–operating temperature conditions. Craters formed due to the convergence of cracks at a node resulted in a delamination region. The delamination area was relatively more for NDP-15 (compare Figs. 10(*a*) and 10(*c*)). This was attributed to lower restriction to the propagation of cracks generated as a result of applied load. Due to the easy propagation

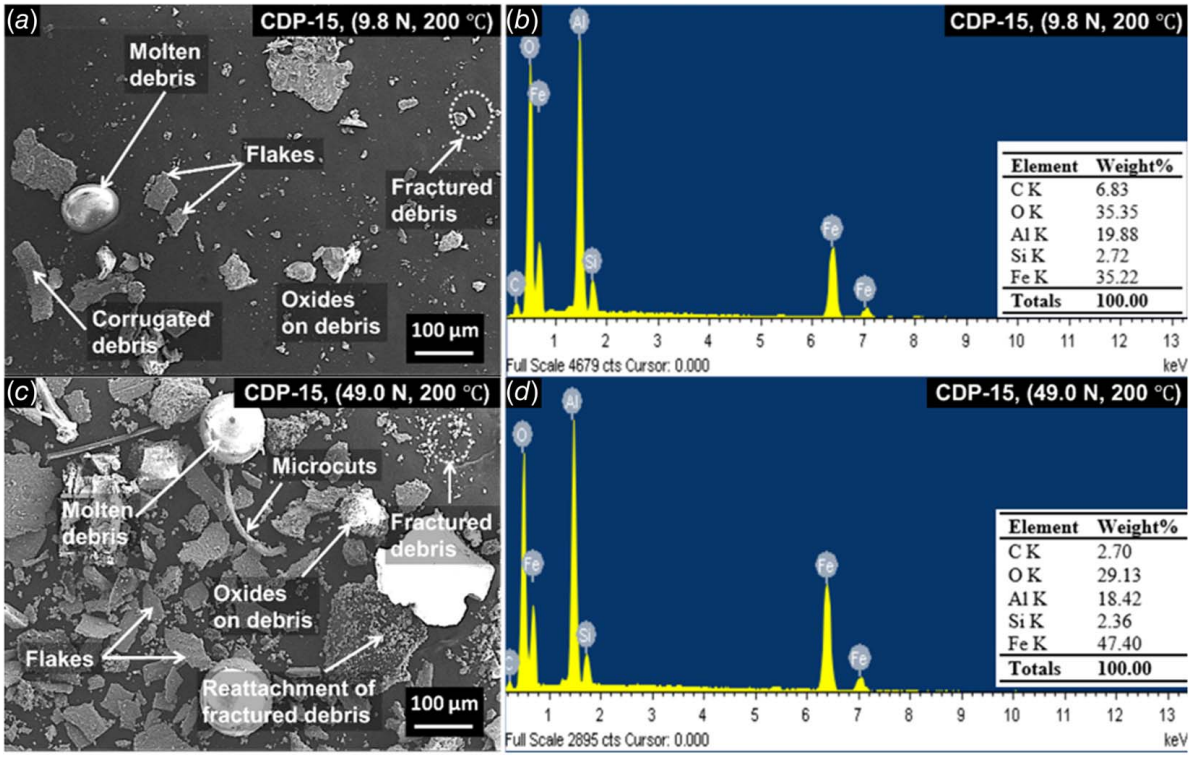

Fig. 11 SEM-EDS of wear debris of CDP-15 obtained at 200 °C for (*a*) and (*b*) 9.8 N and (*c*) and (*d*) 49.0 N

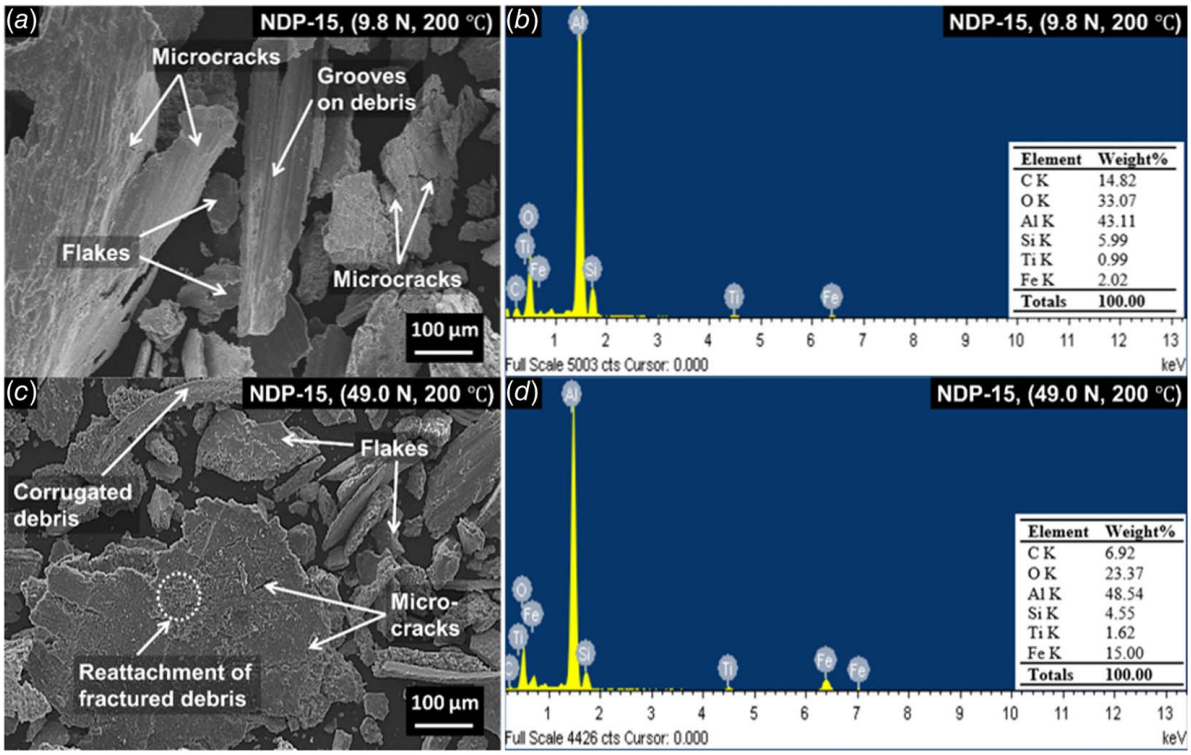

Fig. 12 SEM-EDS of wear debris of NDP-15 at 200 °C for (*a*) and (*b*) 9.8 N and (*c*) and (*d*) 49.0 N

of cracks, the tendency of convergence of cracks increased, which resulted in the high area of the delaminated region. EDS analysis showed a high amount of iron and oxygen content on the worn surface of CDP-15 (Figs. 10(*a*) and 10(*c*)), which was attributed to increased stability of MML in CDPs.

Figures 11 and 12 present the SEM-EDS of worn debris of CDP-15 and NDP-15, respectively, under extreme loads of 9.8 N and 49 N at an operating temperature of 200 °C.

Worn debris of both types of AMCs consisted mainly of flake-like debris. At a low load (9.8 N), the presence of flake-like debris was because of the removal of wedges formed due to

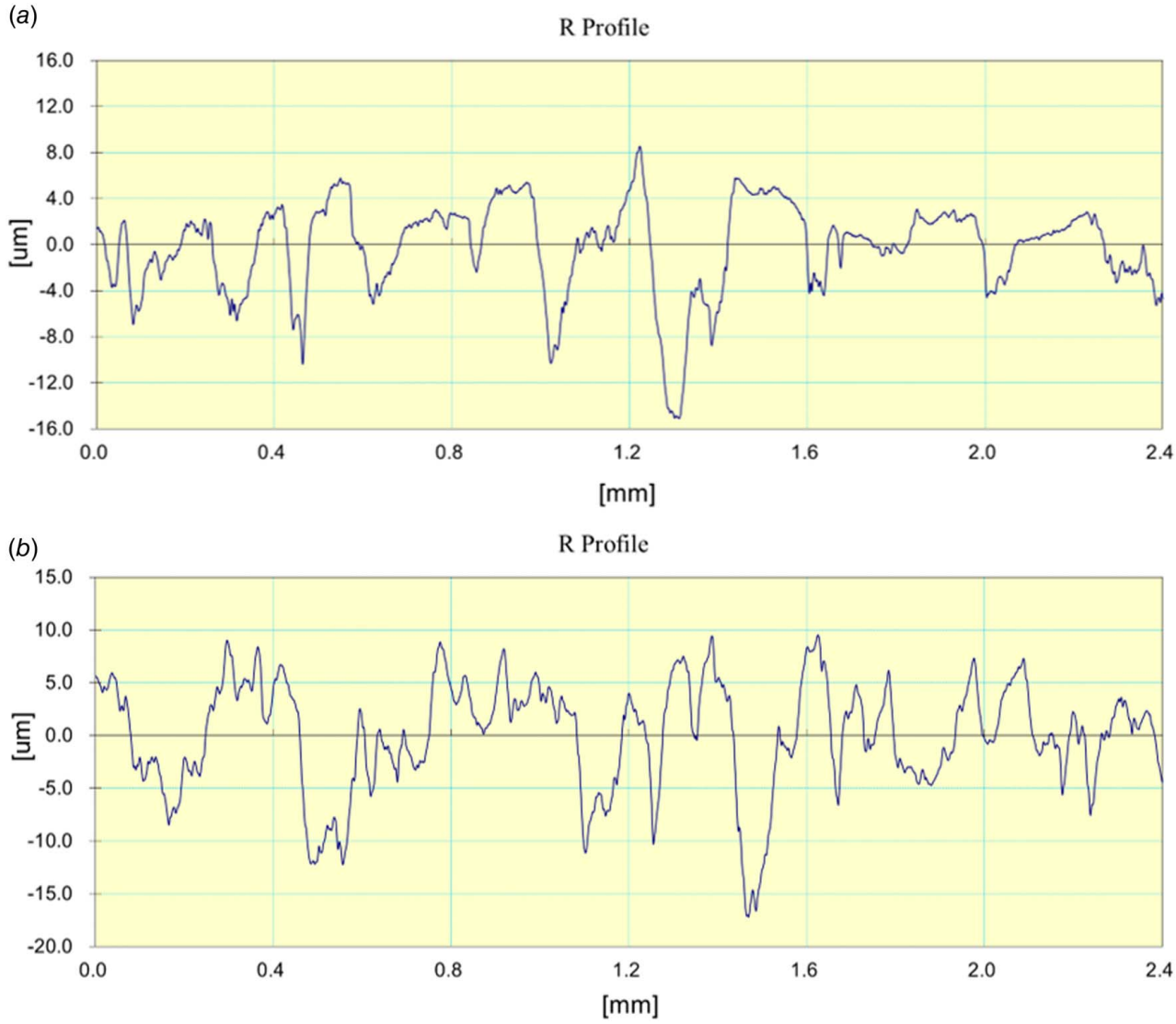

Fig. 13 Roughness profiles of worn surfaces of CDP-15 composites at (*a*) 9.8 N and 200 °C and (*b*) 49.0 N and 200 °C

abrasive wear, which resulted in small-sized debris (Figs. 11(*a*) and 12(*a*)) [18]. For NDP-15, the presence of micro-cracks on flake-like debris was due to plastic deformation of the sliding pin surface as a result of applied load. The presence of plowing marks on flakes represented that after initial abrasive action, removal of material occurred due to the convergence of micro-cracks. For CDP-15, additional features like corrugated debris (due to repetitive stress), molten debris, oxide on debris, and fractured debris (due to applied load conditions) were also observed [17]. The presence of corrugated debris was attributed to adherence of wear debris to the sliding surface and undergoing the repetitive action of stresses. Similarly, when the sliding surface reaches the semisolid state due to frictional heating, molten debris is formed. This frictional heat is also responsible for the formation of oxides on MML, which gets removed to form oxide on debris. During the sliding of surfaces, some of the debris got trapped between the pin and disc surface, which under the action of applied load got fractured and resulted in the formation of fractured debris. Further, under high-load conditions (49 N), relatively large-sized debris was formed due to the convergence of cracks (Figs. 11(*b*) and 12(*b*)). Fractured particles were seen attached to flake-like debris for both types of AMCs, which signified the formation of MML on the sliding surface. CDP-15 showed thread-like debris (due to entrapment of fractured asperities) and molten debris (due to thermal softening of material). As explained earlier, during sliding wear, some debris got trapped between the sliding surfaces. These trapped particles can act as abrasive particles, which results in the formation of thread-like debris.

EDS analysis of worn debris also indicated the presence of silicon, aluminum, oxygen, titanium, iron, and carbon (Figs. 11 and 12). The presence of these elements in debris signified the formation/removal of MML during the sliding wear.

The increase in plastic deformation and intensity of the wear mechanism was justified by measuring the roughness of sliding surfaces. The average roughness (R_a) value obtained for the composite samples (CDP and NDP composites) before the wear test was $1.23 \pm 0.5\ \mu$m. Figure 13 represents the R profile of worn surfaces of CDP-15 obtained for different applied loads. R_a values for the worn surface of CDP-15 at 9.8 N and 49.0 N were observed to be $3.03 \pm 0.41\ \mu$m and $4.15 \pm 0.36\ \mu$m, respectively. The R profile of NDP-15 is shown by Fig. 14. R_a values corresponding to the worn surface of NDP-15 composite were $3.57 \pm 0.29\ \mu$m and $4.78 \pm 0.39\ \mu$m, respectively. For a particular type of reinforcement (viz. boron carbide or ilmenite), the increase in roughness values with the rise in applied load signified higher deformation of the sliding surface. This higher deformation resulted in the formation of large craters by undergoing delamination wear, whereas lower deformation at a lower applied load was attributed to the plowing action caused by

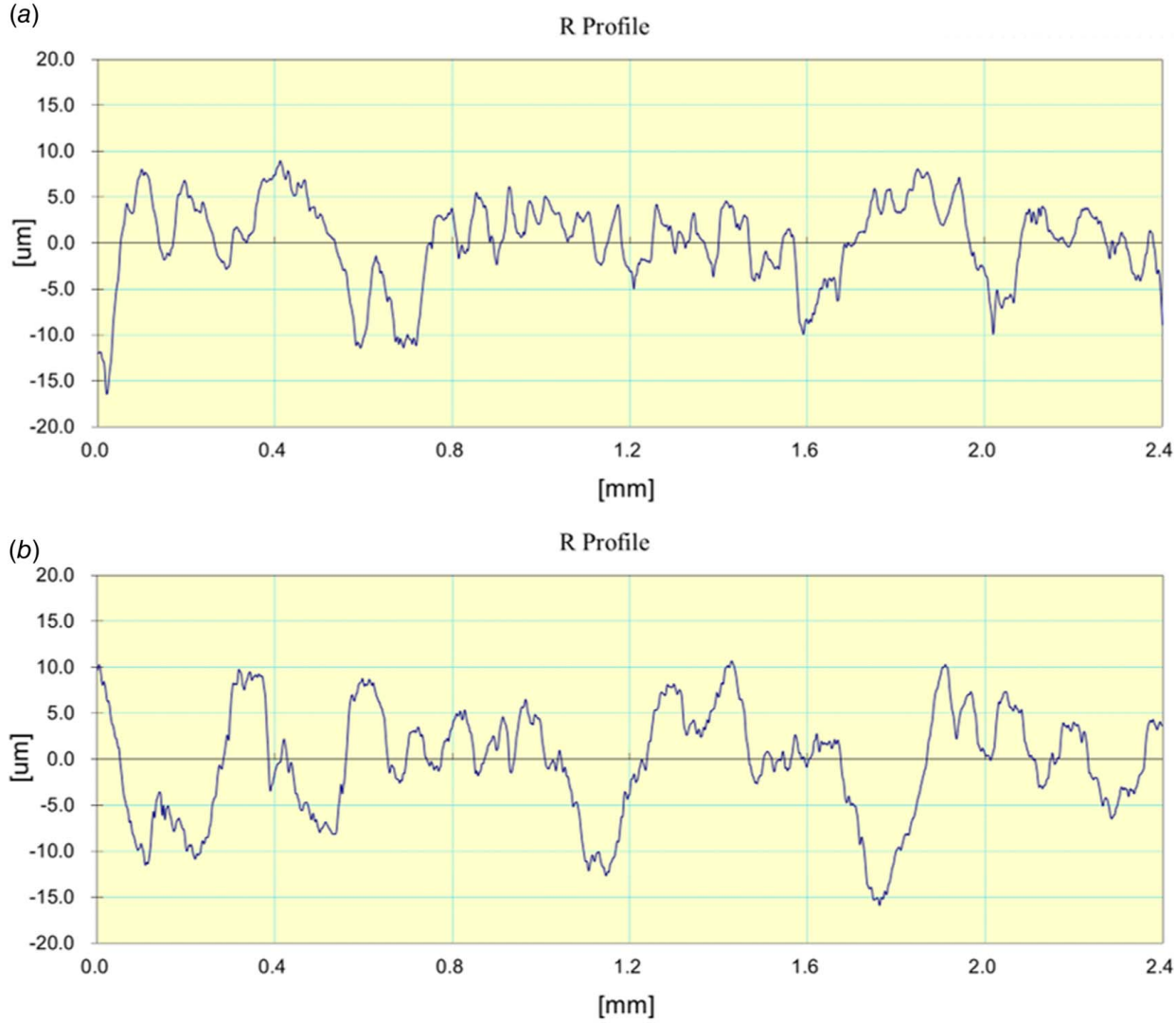

Fig. 14 Roughness profiles of worn surfaces of NDP-15 composites at (*a*) 9.8 N and 200 °C and (*b*) 49.0 N and 200 °C

trapped debris. At particular applied load, NDP-15 composite showed a higher value of roughness in comparison to CDP-15 composite. This signified that the higher intensity of delamination and plowing action led to a higher wear-rate in the case of NDP-15 composite.

4 Conclusions

Efforts for developing high wear-resistant and very low-cost mineral particle–reinforced AMCs (here, NDPs) for high-temperature dry sliding wear applications were successful. The wear behavior of "LM13 + $x$$B_4C$" and "LM13 + $x$$FeTiO_3$" AMCs was compared under elevated temperature conditions. Boron carbide and ilmenite particles were uniformly dispersed in their respective AMCs and caused refinement of primary aluminum and eutectic silicon present in the matrix material. Particle reinforcement of both types improved the hardness and reduced the CTE, COF, and wear-rate values of resulting AMCs. The transition temperature for mild-to-severe wear also improved significantly. These improvements were a result of differences in the densities, CTE values, and thermal conductivities of matrix and reinforced particles. B_4C particle reinforcement improved the wear resistance of AMCs due to the formation of a stable tribolayer, whereas ilmenite particle reinforcement led to improvement by virtue of early oxidation, which provided a protective coating on the composite surface. Though the mechanisms involved were quite different, both types of reinforcements (synthetic versus mineral type) were comparable in improving the wear performance of AMCs under elevated temperature conditions. Thus, the abundantly available ilmenite can act as a substitute material for synthetic ceramic reinforcements for dry sliding wear applications.

Conflict of Interest

There are no conflicts of interest.

Data Availability Statement

The authors attest that all data for this study are included in the paper.

References

[1] Elwan, M., Fathy, A., Wagih, A., Essa, A. R. S., Abu-Oqail, A., and EL-Nikhaily, A. E., 2020, "Fabrication and Investigation on the Properties of Ilmenite (FeTiO3)-Based Al Composite by Accumulative Roll Bonding," J. Compos. Mater., **54**(10), pp. 1259–1271.
[2] Gautam, G., and Mohan, A., 2016, "Wear and Friction of AA5052-Al3Zr In Situ Composites Synthesized by Direct Melt Reaction," ASME J. Tribol., **138**(2), p. 021602.

[3] Karthikeyan, B., Ramanathan, S., and Ramakrishnan, V., 2010, "Thermo Physical Property Measurement of Metal-Matrix Composites," Mater. Des., **31**, pp. S82–S86.
[4] Gupta, R., Nanda, T., and Pandey, O. P., 2021, "Comparison of Wear Behaviour of LM13 Al–Si Alloy Based Composites Reinforced With Synthetic (B4C) and Natural (Ilmenite) Ceramic Particles," Trans. Nonferrous Met. Soc. China, **31**(12), pp. 3613–3625.
[5] Abbas, A., and Huang, S.-J., 2020, "Qualitative and Quantitative Investigation of As-Cast and Aged CNT/AZ31 Metal Matrix Composites," JOM, **72**(6), pp. 2272–2282.
[6] Islam, A., Dwivedi, S. P., Yadav, R., and Dwivedi, V. K., 2021, "Development of Aluminium Based Composite by Utilizing Industrial Waste and Agro-Waste Material as Reinforcement Particles," J. Inst. Eng. (India): Ser. D, **102**(2), pp. 317–330.
[7] Gupta, R., Nanda, T., and Pandey, O. P., 2023, "Tribological Properties of Hybrid Aluminium Matrix Composites Reinforced With Boron Carbide and Ilmenite Particles for Brake Rotor Applications," Arch. Civ. Mech. Eng., **23**(1), pp. 1–18.
[8] Hosseini, V. A., Shabestari, S. G., and Gholizadeh, R., 2013, "Study on the Effect of Cooling Rate on the Solidification Parameters, Microstructure, and Mechanical Properties of LM13 Alloy Using Cooling Curve Thermal Analysis Technique," Mater. Des., **50**, pp. 7–14.
[9] Saghafian, H., Shabestari, S. G., Ghadami, S., and Ghoncheh, M. H., 2017, "Effects of Iron, Manganese, and Cooling Rate on Microstructure and Dry Sliding Wear Behavior of LM13 Aluminum Alloy," Tribol. Trans., **60**(5), pp. 888–901.
[10] Gupta, R., Nanda, T., and Pandey, O. P., 2022, "Effect of High Operating Temperatures on the Wear Characteristics of Boron Carbide and Ilmenite Reinforced LM13 Alloy Based Composites," ASME J. Tribol., **144**(10), p. 101703.
[11] Shabani, M. O., and Mazahery, A., 2011, "Prediction of Wear Properties in A356 Matrix Composite Reinforced With B4C Particulates," Synth. Met., **161**(13–14), pp. 1226–1231.
[12] Nemati, N., Emamy, M., Penkov, O. V., Kim, J., and Kim, D., 2016, "Mechanical and High Temperature Wear Properties of Extruded Al Composite Reinforced With Al13Fe4 CMA Nanoparticles," Mater. Des., **90**, pp. 532–544.
[13] Palanivel, R., Dinaharan, I., Laubscher, R. F., and Davim, J. P., 2016, "Influence of Boron Nitride Nanoparticles on Microstructure and Wear Behavior of AA6082/TiB2 Hybrid Aluminum Composites Synthesized by Friction Stir Processing," Mater. Des., **106**, pp. 195–204.
[14] Gupta, R., Nanda, T., and Pandey, O. P., 2023, "Tribological Characteristics of LM13 Alloy Based Ilmenite-Boron Carbide Reinforced Hybrid Composites for Brake Drum Applications," Wear, **522**, p. 204851.
[15] Ravikumar, K., Kiran, K., and Sreebalaji, V. S., 2017, "Characterization of Mechanical Properties of Aluminium/Tungsten Carbide Composites," Measurement, **102**, pp. 142–149.
[16] Sharma, S. K., Saxena, K. K., and Kumar, N., 2022, "Effect of SiC on Mechanical Properties of Al-Based Metal Matrix Composites Produced by Stir Casting," Met. Sci. Heat Treat., **64**(5–6), pp. 316–320.
[17] Sharma, S., Gupta, R., Nanda, T., and Pandey, O. P., 2021, "Influence of Two Different Range of Sillimanite Particle Reinforcement on Tribological Characteristics of LM30 Based Composites Under Elevated Temperature Conditions," Mater. Chem. Phys., **258**, p. 123988.
[18] Gupta, R., Sharma, S., Nanda, T., and Pandey, O. P., 2020, "Wear Studies of Hybrid AMCs Reinforced With Naturally Occurring Sillimanite and Rutile Ceramic Particles for Brake-Rotor Applications," Ceram. Int., **46**(10B), pp. 16849–16859.
[19] Yang, C. C. T., and Wei, W. C. J., 2000, "Effects of Material Properties and Testing Parameters on Wear Properties of Fine-Grain Zirconia (TZP)," Wear, **242**(1–2), pp. 97–104.
[20] Gupta, R., Sharma, S., Nanda, T., and Pandey, O. P., 2020, "A Comparative Study of Dry Sliding Wear Behaviour of Sillimanite and Rutile Reinforced LM27 Aluminium Alloy Composites," Mater. Res. Express, **7**(1), p. 016540.
[21] Wilson, N. C., Muscat, J., Mkhonto, D., Ngoepe, P. E., and Harrison, N. M., 2005, "Structure and Properties of Ilmenite From First Principles," Phys. Rev. B, **71**(7), p. 075202.
[22] Singhal, V., Gupta, A., Pandey, O. P., Sharma, D., and Kumar Jain, V., 2023, "Investigate the Optical and Dry Sliding Wear Behavior of Solid Lubricated Sillimanite Reinforced Aluminum Metal Matrix Composite," Mater. Today: Proc.
[23] Gupta, A., Singhal, V., and Pandey, O. P., 2023, "Study of the Wear Behavior of Dual Solid Lubricant-Induced Ilmenite-Reinforced Hypereutectic Al-Si Alloy Composites," J. Mater. Eng. Perform., (Ref 20).
[24] Kumar, S., Sarma, V. S., and Murty, B. S., 2010, "High Temperature Wear Behavior of Al-4Cu-TiB2 in Situ Composites," Wear, **268**(11–12), pp. 1266–1274.
[25] Kumar, N., Gautam, G., Gautam, R. K., Mohan, A., and Mohan, S., 2016, "High-Temperature Tribology of AA5052/ZrB_2 PAMCs," ASME J. Tribol., **139**(1), p. 011601.
[26] Prasad, R., Kumar, H., Kumar, P., Tewari, S. P., and Singh, J. K., 2021, "Filler Dispersion and Unidirectional Sliding Characteristics of As-Cast and Multi-Pass Friction Stir Processed ZrB2/AA7075 In-Situ Composites," ASME J. Tribol., **143**(8), p. 081701.
[27] Wang, Q. Z., Lin, X., Wen, X. L., Kang, N., and Huang, W. D., 2021, "Microstructure and Wear Behavior of Nano-TiB2p/2024Al Matrix Composites Fabricated by Laser Direct Energy Deposition With Powder Feeding," ASME J. Tribol., **143**(5), p. 051101.
[28] Panwar, R. S., and Pandey, O. P., 2013, "Study of Wear Behavior of Zircon Sand-Reinforced LM13 Alloy Composites at Elevated Temperatures," J. Mater. Eng. Perform., **22**(6), pp. 1765–1775.
[29] Chen, G., Song, Z., Chen, J., Peng, J., and Srinivasakannan, C., 2013, "Evaluation of the Reducing Product of Carbonthermal Reduction of Ilmenite Ores," J. Alloys Compd., **577**, pp. 610–614.
[30] Sımsek, D., and Ozyurek, D., 2020, "The Wear Performance at High Temperatures of ZrO2-Reinforced Aluminum Matrix Composites Produced by Mechanochemical Reaction Method," ASME J. Tribol., **142**(10), p. 101701.
[31] Raghavender, A. T., Hong, N. H., Lee, K. J., Jung, M. H., Skoko, Z., Vasilevskiy, M., Cerqueira, M. F., and Samantilleke, A. P., 2013, "Nano-Ilmenite FeTiO3: Synthesis and Characterization," J. Magn. Magn. Mater., **331**, pp. 129–132.
[32] Kumar, C. A. V., Rajadurai, J. S., and Sundararajan, S., 2016, "Performance Enrichment on Tribological Characteristics of Powder Metallurgy Processed Aluminium Particulate Composites by Inclusion of Rutile (TiO2)," J. Mater. Res., **31**(16), pp. 2445–2456.
[33] Clauser, C., and Huenges, E., 1995, "Thermal Conductivity of Rocks and Minerals," *Rock Physics and Phase Relations: A Handbook of Physical Constants*, Vol. 3, American Geophysical Union, Washington, DC, pp. 105–126.
[34] Abdou, M. I., Al-Sabagh, A. M., Ahmed, H. E., and Fadl, A. M., 2018, "Impact of Barite and Ilmenite Mixture on Enhancing the Drilling Mud Weight," Egypt. J. Pet., **27**(4), pp. 955–967.
[35] Jafrey Daniel, J. D., Babu, L. G., Ramesh, M., and Ravichandran, M., 2019, "Mechanical and Tribological Characteristics of ZrO_2 Reinforced Al2014 Matrix Composites Produced via Stir Casting Route," Mater. Res. Express, **6**(11), p. 115542.
[36] Patel, S. K., Singh, V. P., and Kuriachen, B., 2019, "Microstructural, Tribological and Mechanical Properties Evolution of ZrSiO4/A4047 Surface Composite Fabricated Through Friction Stir Processing," Trans. Indian Inst. Met., **72**(7), pp. 1765–1774.
[37] Alagarsamy, S. V., and Ravichandran, M., 2019, "Synthesis, Microstructure and Properties of TiO_2 Reinforced AA7075 Matrix Composites via Stir Casting Route," Mater. Res. Express, **6**(8), p. 086519.
[38] 1995, "ASTM Standard G-99, Test Method for Wear Testing Using a Pin-on-Disk Apparatus," ASTM Annual Book of Standards, Vol. 03.02, West Conshohocken, PA, 03.
[39] Seong, H. G., Lopez, H. F., Robertson, D. P., and Rohatgi, P. K., 2008, "Interface Structure in Carbon and Graphite Fiber Reinforced 2014 Aluminum Alloy Processed With Active Fiber Cooling," Mater. Sci. Eng. A, **487**(1–2), pp. 201–209.
[40] Tham, L. M., Gupta, M., and Cheng, L., 2001, "Effect of Limited Matrix-Reinforcement Interfacial Reaction on Enhancing the Mechanical Properties of Aluminium-Silicon Carbide Composites," Acta Mater., **49**(16), pp. 3243–3253.
[41] Nie, C., Gu, J., Liu, J., and Zhang, D., 2008, "Investigation on Microstructures and Interface Character of B4C Particles Reinforced 2024Al Matrix Composites Fabricated by Mechanical Alloying," J. Alloys Compd., **454**(1–2), pp. 118–122.
[42] Lasa, L., and Rodriguez-Ibabe, J. M., 2003, "Wear Behaviour of Eutectic and Hypereutectic Al-Si-Cu-Mg Casting Alloys Tested Against a Composite Brake Pad," Mater. Sci. Eng. A, **363**(1–2), pp. 193–202.
[43] Karantzalis, A. E., Lekatou, A., Georgatis, E., and Mavros, H., 2010, "Solidification Behaviour of Ceramic Particle Reinforced Al-Alloy Matrices," J. Mater. Sci., **45**(8), pp. 2165–2173.
[44] Grasso, S., Hu, C., Vasylkiv, O., Suzuki, T. S., Guo, S., Nishimura, T., and Sakka, Y., 2011, "High-Hardness B4C Textured by a Strong Magnetic Field Technique," Scr. Mater., **64**(3), pp. 256–259.
[45] Karantzalis, A. E., Lekatou, A., Georgatis, E., Poulas, V., and Mavros, H., 2010, "Microstructural Observations in a Cast Al-Si-Cu/TiC Composite," J. Mater. Eng. Perform., **19**(4), pp. 585–590.
[46] Singh, G., and Goyal, S., 2018, "Microstructure and Mechanical Behavior of AA6082-T6/SiC/B4C-Based Aluminum Hybrid Composites," Part. Sci. Technol., **36**(2), pp. 154–161.
[47] Shen, Y. L., Williams, J. J., Piotrowski, G., Chawla, N., and Guo, Y. L., 2001, "Correlation Between Tensile and Indentation Behavior of Particle-Reinforced Metal Matrix Composites: An Experimental and Numerical Study," Acta Mater., **49**(16), pp. 3219–3229.
[48] Lalet, G., Kurita, H., Heintz, J. M., Lacombe, G., Kawasaki, A., and Silvain, J. F., 2014, "Thermal Expansion Coefficient and Thermal Fatigue of Discontinuous Carbon Fiber-Reinforced Copper and Aluminum Matrix Composites Without Interfacial Chemical Bond," J. Mater. Sci., **49**(1), pp. 397–402.
[49] Ren, S., He, X., Qu, X., Humail, I. S., and Li, Y., 2007, "Effect of Mg and Si in the Aluminum on the Thermo-Mechanical Properties of Pressureless Infiltrated SiCp/Al Composites," Compos. Sci. Technol., **67**(10), pp. 2103–2113.
[50] Zhang, Q., Wu, G., Jiang, L., and Chen, G., 2003, "Thermal Expansion and Dimensional Stability of Al-Si Matrix Composite Reinforced With High Content SiC," Mater. Chem. Phys., **82**(3), pp. 780–785.
[51] Jiang, T., Li, S., Yu, C., Fu, J., Wei, B., Luo, L., and Xu, G., 2019, "The Evolution on the Microstructure and Thermal Expansion Behavior of Al–50Si Alloy With Different P Contents," J. Mater. Sci. Mater. Electron., **30**(7), pp. 6786–6794.
[52] Di Giovanni, M. T., De Menezes, J. T. O., Cerri, E., and Castrodeza, E. M., 2020, "Influence of Microstructure and Porosity on the Fracture Toughness of Al-Si-Mg Alloy," J. Mater. Res. Technol., **9**(2), pp. 1286–1295.
[53] Torres, H., Varga, M., Adam, K., and Ripoll, M. R., 2016, "The Role of Load on Wear Mechanisms in High Temperature Sliding Contacts," Wear, **364–365**, pp. 73–83.